Chapter 4: Multiscale and Multilevel Modeling of Composites

Young W. Kwon

Naval Postgraduate School, Monterey, CA, USA

4.1 Introduction

Composites have been used increasingly in various engineering applications which include, but are not limited to, the aerospace, automobile, sports, and leisure industries. To improve properties of composites so that they become stronger, stiffer, tougher, refractory, etc., it would be very useful to design the composite materials from the atomic levels. This requires proper multiscale and multilevel modeling techniques so that those techniques can be used for the design stage of new composites as well as the analysis of existing composites. This chapter presents multiscale and multilevel modeling techniques for different kinds of composite architectures which include particle-reinforced, fiber-reinforced, and woven fabric composites. The following sections describe these techniques.

4.2 Particulate Composites

4.2.1 Multiscale Analysis for Particulate Composites

A particle-reinforced composite, or particulate composite, is one of the simplest forms of composites. It has particles embedded in a matrix material. As a result, the multiscale analysis hierarchy is simple for the particulate composite, as illustrated in Fig. 4.1. The analysis connects the microscale, such as particles and matrix, to the mesoscale, such as the representative particulate composite, and finally to macroscale composites, such as a particulate composite structure [13, 23–32]. The multiscale analysis has

two routes which complement each other for a complete cycle of analysis. The first route is the Stiffness Loop, and the other is the Stress Loop. For the Stiffness Loop, effective material properties are computed for an upper scale from material and geometric properties of the neighboring lower scale. For example, the effective particulate composite material properties are calculated from the particle and matrix material and geometric properties. The Particulate Module computes the effective properties, and it is described later. Then, the effective material properties are used for structural analysis of a composite as illustrated in Fig. 4.1.

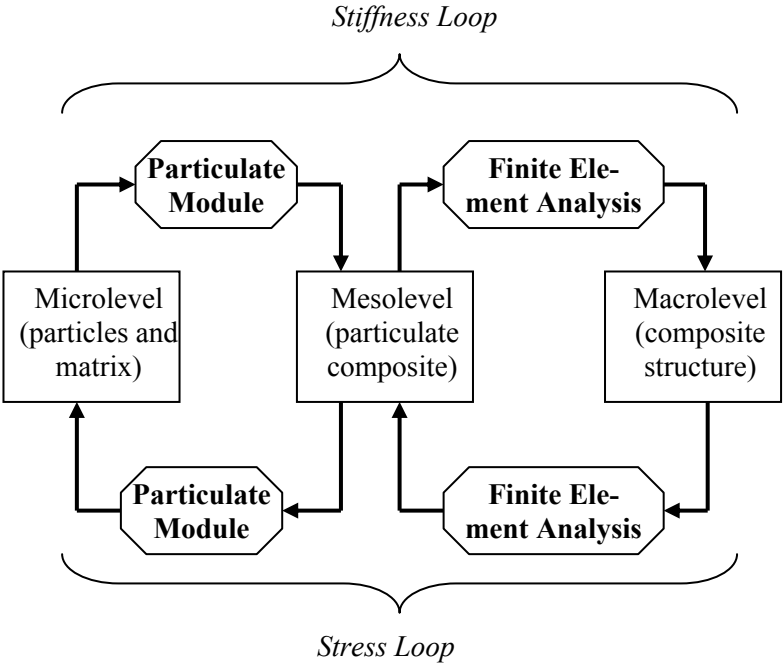

Fig. 4.1. Multiscale analysis hierarchy for a particulate composite

Structural analysis of the composite results in stresses, strains, and displacements at the macroscale. The stresses and strains are the composite level values, i.e., smeared values for the particles and the matrix. It is necessary to decompose the composite structural level stresses and strains into constituent level stresses and strains to apply the damage or failure criteria to the constituent materials, such as the particles and matrix. The same module used for the Stiffness Loop, i.e., Particulate Module is also used to compute the stresses and strains in the particle and matrix.

Sections 4.2.2 and 4.2.3 describe, respectively, the Particulate Module and the damage mechanics and crack initiation criterion used for the study.

4.2.2 Particulate Module

A representative unit cell is used for the present module. The purpose of this module is twofold. The first is to predict the effective stiffness of a particulate composite from the particle and matrix material properties as well as their geometric data. The second is to determine the microlevel stresses and strains occurring in the particle and matrix from the stresses and strains of the composite level. As a result, the module is used for both the Stiffness Loop and the Stress Loop.

To develop a representative unit cell for a particulate composite, a single representing particle surrounded by a matrix material is assumed. In general, every particle may have a different shape; however, the shape of the representative particle is simplified. A spherical shape would be a reasonable assumption. However, for mathematical simplicity, a cubic shape is assumed.

A microscale analysis of different shapes of particles using the boundary element method [20] showed that the effective material properties of the composite were insensitive to the actual shape of the particle. However, the same study indicated that the microscale stresses were rather sensitive to the particle shape. The sensitivity was mostly due to the stress concentration at sharp corners. For actual composites, each particle has a different shape and stress concentration. Practically, there is no way to consider all those different particle shapes and their stress concentration effects. A possible solution to this complex problem is using statistical mechanics. However, that approach is also very time-consuming. If it is assumed that the macro-level failure strength is more or less uniform for test coupons made out of the same particulate composite, the local stress concentration effects due to different shapes of particles may be smeared out in the composite test coupons. In this regard, a more regular shape of particle in the representative unit cell may be considered. Furthermore, the average values of stresses for the representative particle will be computed. This also makes the actual shape of particle less relevant for the unit cell.

Figure 4.2 shows the representative unit cell. With the assumption of symmetry, only one-eighth of the unit cell is shown in the figure, where the representative embedded particle is denoted by subcell *a*. The surrounding matrix material is represented by subcells *b* to *h* as illustrated in the figure. To clearly represent the relative positions of all subcells within the unit cell, the subcells are shown independently in the figure with

lines and springs denoting their connections to neighboring subcells. The lines indicate continuous material between any two neighboring materials while the springs denote any potential interface effect between the particle and the matrix. The spring constant can be adjusted with either a strong or weak interface. The present model can have three different interface material properties along the three directions. However, for an isotropic material and damage behavior, all interface material properties, i.e., the spring constants, will be assumed to be the same. The size of the particle subcell a is $(V_p)^{1/3}$ where V_p is the particle volume fraction of the composite.

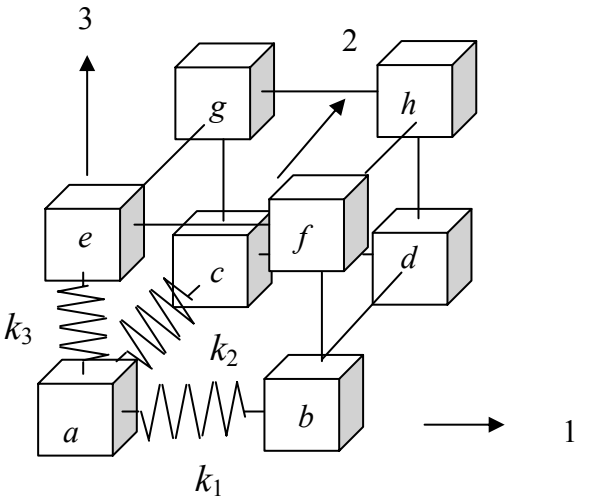

Fig. 4.2. Representative unit cell for a particulate composite

For each subcell, average stresses and strains are considered for the following derivation. Stresses must satisfy the equilibrium between any neighboring subcells as shown below

$$\sigma_{11}^{a} = \sigma_{11}^{b}, \quad \sigma_{11}^{c} = \sigma_{11}^{d}, \quad \sigma_{11}^{e} = \sigma_{11}^{f}, \quad \sigma_{11}^{g} = \sigma_{11}^{h}, \tag{4.1}$$

$$\sigma_{22}^{a} = \sigma_{22}^{c}, \quad \sigma_{22}^{b} = \sigma_{22}^{d}, \quad \sigma_{22}^{e} = \sigma_{22}^{g}, \quad \sigma_{22}^{f} = \sigma_{22}^{h}, \tag{4.2}$$

$$\sigma_{33}^{a} = \sigma_{33}^{e}, \quad \sigma_{33}^{b} = \sigma_{33}^{f}, \quad \sigma_{33}^{c} = \sigma_{33}^{g}, \quad \sigma_{33}^{d} = \sigma_{33}^{h}, \tag{4.3}$$

where superscript denotes the subcell identification as shown in Fig. 4.2 and subscript indicates the stress component. These equations are for normal

components of stresses. Similar equations can be written for shear components, but they are omitted here to save space.

The subcell strains satisfy the following compatibility equations by assuming uniform deformation of the unit cell under periodic boundary conditions

$$l_{\mathrm{p}}\varepsilon_{11}^{a}+l_{\mathrm{m}}\varepsilon_{11}^{b}+\left(l_{\mathrm{p}}^{2}\sigma_{11}^{a}/k_{1}\right)=l_{\mathrm{p}}\varepsilon_{11}^{c}+l_{\mathrm{m}}\varepsilon_{11}^{d}=l_{\mathrm{p}}\varepsilon_{11}^{e}+l_{\mathrm{m}}\varepsilon_{11}^{f}=l_{\mathrm{p}}\varepsilon_{11}^{g}+l_{\mathrm{m}}\varepsilon_{11}^{h}, \quad (4.4)$$

$$l_{\mathrm{p}}\varepsilon_{22}^{a}+l_{\mathrm{m}}\varepsilon_{22}^{c}+\left(l_{\mathrm{p}}^{2}\sigma_{22}^{a}/k_{2}\right)=l_{\mathrm{p}}\varepsilon_{22}^{b}+l_{\mathrm{m}}\varepsilon_{22}^{d}=l_{\mathrm{p}}\varepsilon_{22}^{e}+l_{\mathrm{m}}\varepsilon_{22}^{g}=l_{\mathrm{p}}\varepsilon_{22}^{f}+l_{\mathrm{m}}\varepsilon_{22}^{h}, \quad (4.5)$$

$$l_{\mathrm{p}}\varepsilon_{33}^{a}+l_{\mathrm{m}}\varepsilon_{33}^{e}+\left(l_{\mathrm{p}}^{2}\sigma_{33}^{a}/k_{3}\right)=l_{\mathrm{p}}\varepsilon_{33}^{b}+l_{\mathrm{m}}\varepsilon_{33}^{f}=l_{\mathrm{p}}\varepsilon_{33}^{c}+l_{\mathrm{m}}\varepsilon_{33}^{g}=l_{\mathrm{p}}\varepsilon_{33}^{d}+l_{\mathrm{m}}\varepsilon_{33}^{h}, \quad (4.6)$$

where

$$l_{\mathrm{p}}=V_{\mathrm{p}}^{1/3}, \quad (4.7)$$

$$l_{\mathrm{m}}=1-l_{\mathrm{p}}. \quad (4.8)$$

Other necessary mathematical expressions are constitutive equations for the particle and matrix materials as well as for the composite. For the present particulate composite material, both constituent materials and the effective composite material are considered as isotropic materials. Furthermore, the unit cell stresses and strains are assumed to be the volume averages of subcell stresses and strains

$$\bar{\sigma}_{ij}=\sum_{n}V^{n}\sigma_{ij}^{n}, \quad (4.9)$$

$$\bar{\varepsilon}_{ij}=\sum_{n}V^{n}\varepsilon_{ij}^{n}, \quad (4.10)$$

where superimposed bar denotes the composite (unit cell level) stresses and strains, and V^{n} is the volume fraction of the *n*th subcell. The summation is over all subcells.

Algebraic manipulation of the previous equations finally yields the two main expressions as given below

$$[E^{\mathrm{eff}}]=[V][E][R], \quad (4.11)$$

$$\{\varepsilon\}=[R]\{\bar{\varepsilon}\}, \quad (4.12)$$

in which $[E^{\mathrm{eff}}]$ is the effective composite material property matrix, $[V]$ is the matrix composed of subcell volume fractions, $[E]$ is the matrix consisting of constituent material properties, and $[R]$ is the matrix relating the subcell

strain vector consisting of particle and matrix strains $\{\varepsilon\}$ to the unit cell strain vector (effective composite strain) $\{\overline{\varepsilon}\}$.

Equation (4.11) is used for the Stiffness Loop while (4.12) is used for the Stress Loop. Once the microlevel strains are computed from (4.12), the constitutive equation of the particle and matrix material, respectively, is used at the microlevel to compute the microlevel stresses. Then, damage and failure criteria are applied to the microlevel stresses and strains.

4.2.3 Damage Mechanics and Crack Initiation Criterion

One of the advantages of applying damage and failure criteria at the microlevel is that even if the composite material has a different particle volume fraction, it is not necessary to obtain new composite material strength data from an experiment. Furthermore, all damage or failure modes can be simplified at the microlevel so that the damage or failure mechanism can be understood more clearly. For example, damage in a particulate composite can be classified into three categories as illustrated in Fig. 4.3: particle breakage, matrix cracking, and particle/matrix interface debonding. The interface debonding may be considered as matrix cracking at the boundary of particles. Different damage or failure criteria may be used for different damage or failure modes. For example, an isotropic damage theory can be applied to the matrix material if the material is isotropic and the damage progression is also assumed to be isotropic.

An experimental study of crack initiation and growth from a round notch tip in a composite showed that a crack initiated at the notch tip and

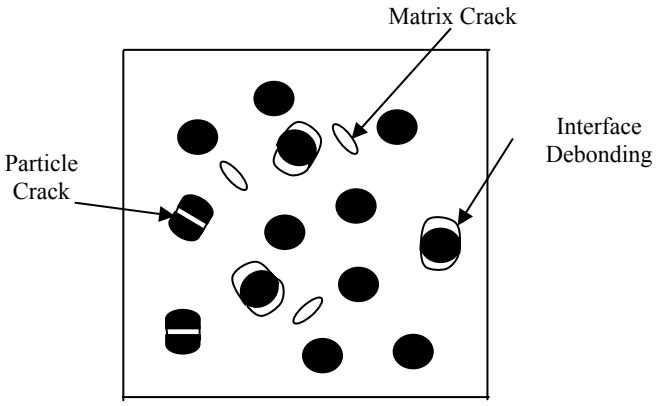

Fig. 4.3. Different damage at the microlevel of a particulate composite

grew until it reached a certain size. Then, the crack tip became blunted for a while until it propagated further. Using the computational model, it was hoped to predict the initial crack length before blunting and subsequent crack propagation. The crack size before the initial blunting is called the initial crack length. To predict such an initial crack size, the damage mechanics were used along with the criterion described below.

Let us consider a perforated plate under tension. Because of stress concentration, the stress very near the hole is much greater than the nominal value. Such high stress occurring very near the hole also results in damage at that location earlier than other locations. As the damage progresses very near the hole, the material at the same location becomes softer with greater damage. This means that even though the strain at very near the hole continues to grow with damage growth, the stress at the same location becomes lower with softer materials. Eventually, the stress very near the hole becomes lower than that in other locations until the stress at the tip of the hole goes down to nil. Such a process for stress reduction along with an increase of damage is illustrated in Fig. 4.4.

The case in Fig. 4.4d indicates damage saturation at the edge of the hole so that the stress there becomes nil. This means a crack can initiate from the hole edge at the onset of damage saturation. Then, the main question for the initial crack size is how far the crack will propagate from the initiation to form an initial crack before blunting. To answer this question, the material behavior near the hole edge is examined. This investigation shows that the material very near the hole edge has material softening. In other words, the slope of the stress–strain curve at the material softening zone becomes negative. This implies that the material softening zone is unstable. As a result, the crack initiated at the hole edge at the onset of damage saturation is expected to grow through the unstable material zone. This indicates that the initial crack size is equal to the length of the unstable material zone in front of the hole edge, as indicated by l_c in Fig. 4.4d. In summary, the criterion to predict the initial crack length is stated below:

At the onset of damage saturation at the edge of a hole, i.e., the stress becomes nil at that location, the length of the unstable material zone, i.e., material softening zone, is the initial crack size.

This criterion was tested against experimental data. The predicted results agreed very well with experimental results. For example, a particulate composite made of hard particles embedded in a very soft matrix

material was studied. In this case, because particles are much stronger than the matrix material, a crack formed in the matrix material. Hence, the multiscale technique described in Sect. 4.2.1 was applied to the particulate composite, and the damage mechanics along with the proposed initial crack length criterion was applied to the matrix material level stresses and strains. The difference between the experimental and predicted results of the initial crack lengths formed at the edge of holes was almost uniformly between 5 and 10%. Figure 4.5 shows an initial crack formed in a particulate composite [30, 31].

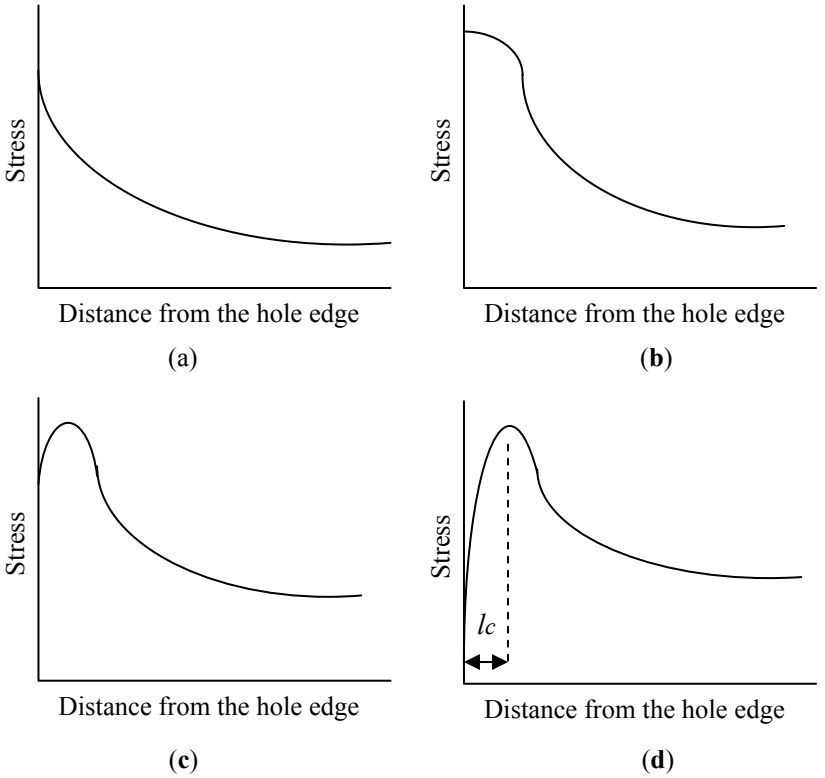

Fig. 4.4. Stress plots from the edge of a hole. Each stress plot from (**a**) to (**d**) is associated with increase of damage very near the hole along with load increase: (**a**) no damage state, (**b**) and (**c**) progressive damage states, and (**d**) saturated damage state

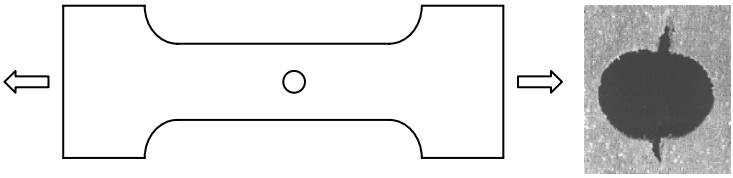

Fig. 4.5. Specimen under tensile loading. The figure on the *right* shows initial cracks formed at the edges of the hole

4.2.4 Study of Microstructural Inhomogeneity

Because the multiscale technique presented previously uses the material properties at the constituent material level, i.e., microscale level, it is easy to model inhomogeneous microstructure, such as a nonuniform particle distribution inside a composite. Even if the overall stiffness of a composite is much less dependent on the actual particle distribution, the effective strength of the composite depends on the particle distribution. For different particle distributions of the same amount of volume fraction, result in different local stresses which control failure at different load levels.

An experimental study was conducted for a particulate composite to determine the particle distribution. In this study, a large square specimen was cut into smaller sizes of square specimens subsequently. Then, at each level of cutting, the same sizes of specimens were examined using an X-ray technique to measure the particle volume fraction of every respective specimen. If the particle volume fraction were uniform in the original specimen, all smaller specimens would have the same particle volume fraction. However, as expected in a real specimen, there was a deviation of the particle volume fraction which is directly related to the mean intensity of the X-ray passing through each composite specimen. Therefore, the standard deviation was computed for each size of small samples. The study indicated that as the specimen size became smaller than a critical size, the standard deviation of the mean intensity of X-ray began to increase significantly. This result implies that an average particle distribution is quite uniform over a domain size greater than a critical size.

To model such an inhomogeneity of particle distribution, a composite specimen was divided into a number of domains with each domain size equal to the critical size. Then, the particle volume fraction was assumed to be the same for each domain. Every domain was further divided into much smaller subdomains. Particle volume fractions were varied randomly

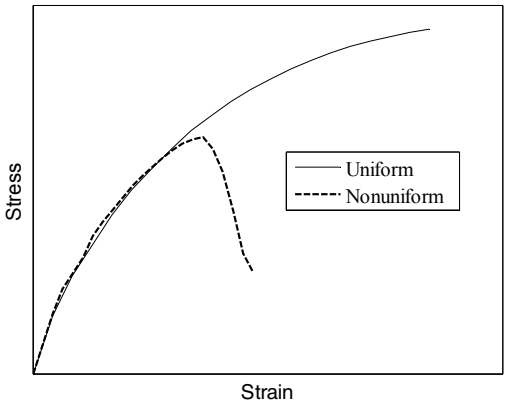

Fig. 4.6. Comparison of stress–strain curves for uniform and nonuniform particle distribution cases

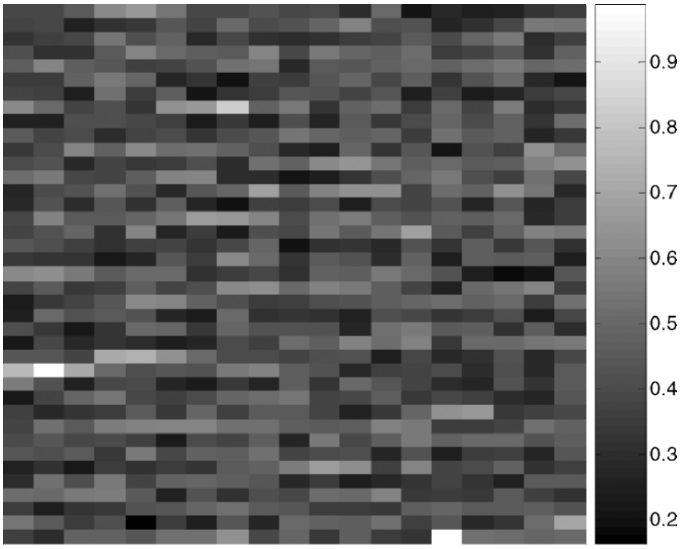

(**a**)

Fig. 4.7. (continue)

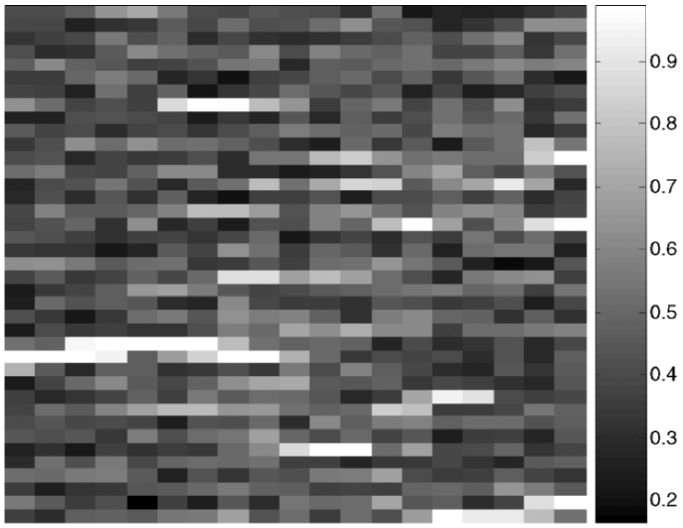

(**b**)

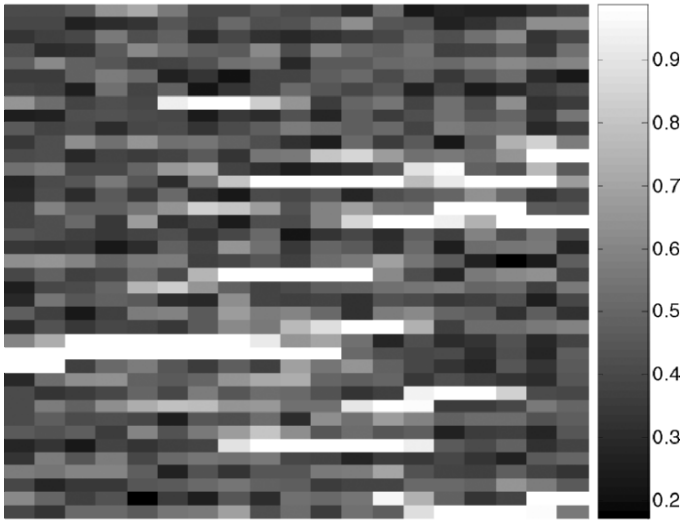

(**c**)

Fig. 4.7. Progressive damage plot from (**a**) lower damage state to (**c**) higher damage state. *White lines* indicate damage saturation, i.e., cracks

among subdomains within each domain while the average particle volume fraction was equal to the domain particle volume fraction. By doing so, local stress effect due to inhomogeneous microstructure in a composite can be studied [28, 31].

Comparing the stress–strain curves between uniform and nonuniform particle distribution cases for the whole specimen, the nonuniform distribution case resulted in much lower failure strength and strain values as illustrated in Fig. 4.6. A nonuniform particle distribution resulted in locally higher stresses and strains than the uniform case. This caused crack initiations earlier for the nonuniform case and eventually earlier failure as shown in Fig. 4.7. The figure plots damage parameter distributions as damage increases. The lighter color in the gray scale indicates a greater damage state. The highest damage is represented by white, which denotes cracks.

This study also provided information regarding what would be a useful failure criterion for such a composite discussed above. Because the composite has much stronger and stiffer particles than the matrix, failure in the matrix did not affect much the effective stress at the composite level. Hence, the composite stresses would not be a good choice for a failure criterion at the macrolevel. On the other hand, the composite strains represent the damage very closely, and would be a good selection for a failure criterion at the macrolevel.

4.3 Fibrous Composites

4.3.1 Multiscale Analysis for Fibrous Composites

Fiber-reinforced composites can be constructed by multiple layers. Every layer has long unidirectional fibers embedded in a matrix material, and the fiber orientation of each layer is generally varied from layer to layer. For the fibrous composite, the multiscale analysis hierarchy is depicted in Fig. 4.8. Comparing to the particulate composite, the fibrous composite requires one more step for the multiscale analysis, which is the Lamination Module [7, 14–16, 19].

As illustrated in Fig. 4.8, the overall hierarchy has a Stiffness Loop and a Stress Loop for a complete cycle. The same modules are also used for both loops. First of all, the fiber and matrix material and geometric properties are used in the Fibrous Module to determine the effective

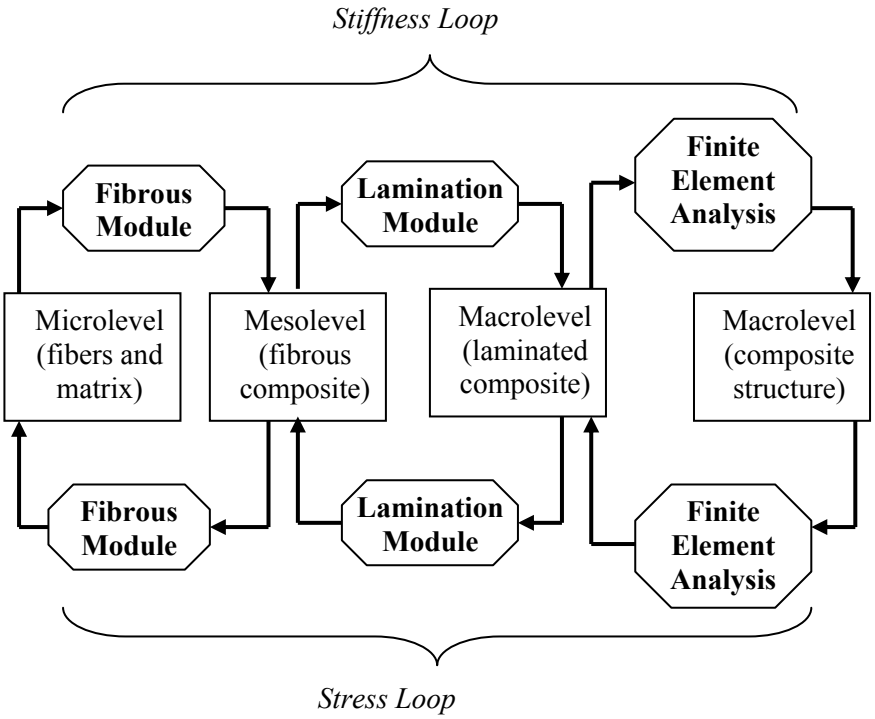

Fig. 4.8. Multiscale analysis hierarchy for a fibrous composite

material properties of a unidirectional fibrous composite. These composite properties are used for each lamina with its orientation of fibers with respect to the global coordinate system. The "Lamination Module" computes the effective properties of the laminated composite. Then, those properties are used for finite element analysis of a laminated composite structure. This completes the Stiffness Loop. Then, the reverse order is used to decompose stresses and strains at the macrolevel into those in the microlevel, i.e., stresses and strains in the fiber and matrix materials.

Once microlevel stresses and strains are computed, damage and/or failure criteria are applied to them. Because damage and failure are described at the constituent level, damage and failure modes are simplified and physics-based. At the microlevel, there are three potential damages and failures: fiber breakage, matrix cracking, and interface debonding. Different damage or failure criteria can be applied to those three different damage modes.

At the macrolevel, there are more complicated damage modes. For example, interlamina delamination, matrix cracking in a crossply lamina, and fiber splitting in a longitudinal layer are some of potential damage modes. All of these are associated with matrix cracking. Depending on the location of the matrix failure and its orientation to the layer and fiber orientations, the damage modes are differentiated as described above. For the macrolevel damage or failure criteria, each of those modes may require a different criterion and failure strength. However, when using the constituent level damage or failure criteria, all of those can be described using the same criterion associated with matrix damage. Simply, the damage or failure location and orientation will dictate the difference at the macroscale failure modes. As a result, damage and failure modes can be understood in unified and simplified concepts.

One of the advantages of the multiscale analysis technique is its flexibility for adaptation. For instance, if the fiber volume fraction was varied at the average sense or locally, the same multiscale technique can be used without any modification. It is not necessary to measure experimentally new strength and stiffness associated with the new volume fraction. Section 4.3.2 presents the modules used for the multiscale analysis of fibrous composites.

4.3.2 Fibrous Module

The Fibrous Module is based on a representative unit cell which contains a representative fiber surrounded by a matrix material. The fiber and matrix materials have, in general, significantly different properties. This is also true for the coefficients of thermal expansion. Due to this mismatch, thermal stresses arise at the micro level between the fiber and matrix. To minimize such thermal stresses, the fiber/matrix interface is designed to have a weak layer of bonding and slide each other as necessary. In this case, it would be beneficial to include the fiber/matrix interface layer in the representative unit cell model [10].

The unit cell model is shown in Fig. 4.9. The unit cell has a representative fiber along the x-axis, and cross-section containing the representative fiber, interface layer, and the matrix material in the y–z plane. Mostly, the fiber materials are elastic up to fracture while the matrix materials may be elastic, viscoelastic, or elastoplastic [3–6, 17]. As a result, an incremental formulation is presented here to incorporate inelastic deformation.

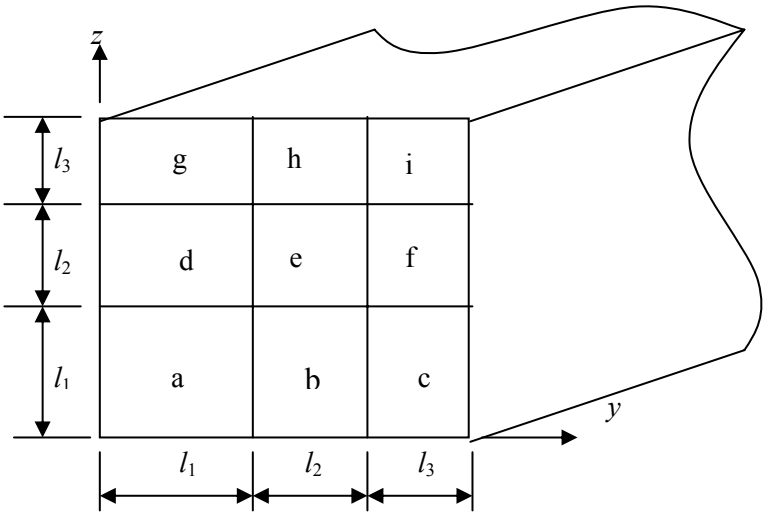

Fig. 4.9. Representative unit cell for a fibrous composite

To derive expressions to compute effective material properties for the Stiffness Loop and the stress decomposition for the Stress Loop, the following stress equilibrium of subcells is considered for the normal stress components

$$\begin{aligned} &\Delta\sigma_y^a = \Delta\sigma_y^b, \quad \Delta\sigma_y^b = \Delta\sigma_y^c, \quad \Delta\sigma_y^d = \Delta\sigma_y^e, \\ &\Delta\sigma_y^e = \Delta\sigma_y^f, \quad \Delta\sigma_y^g = \Delta\sigma_y^h, \quad \Delta\sigma_y^h = \Delta\sigma_y^i, \end{aligned} \tag{4.13}$$

$$\begin{aligned} &\Delta\sigma_z^a = \Delta\sigma_z^d, \quad \Delta\sigma_z^d = \Delta\sigma_z^g, \quad \Delta\sigma_z^b = \Delta\sigma_z^e, \\ &\Delta\sigma_z^e = \Delta\sigma_z^h, \quad \Delta\sigma_z^c = \Delta\sigma_z^f, \quad \Delta\sigma_z^f = \Delta\sigma_z^i, \end{aligned} \tag{4.14}$$

where superscripts are used to identify the subcells and stresses are assumed to be uniform within each subcell. Similar expressions can be developed for the shear stress components. The first set of equations is equilibrium in the *y*-axis and the second set is for the *z*-axis.

The deformation compatibilities among subcells are expressed as followed for the *y*- and *z*-axis, respectively

$$\begin{aligned} l_1\Delta\varepsilon_y^a + l_2\Delta\varepsilon_y^b + l_3\Delta\varepsilon_y^c &= l_1\Delta\varepsilon_y^d + l_2\Delta\varepsilon_y^e + l_3\Delta\varepsilon_y^f \\ &= l_1\Delta\varepsilon_y^g + l_2\Delta\varepsilon_y^h + l_3\Delta\varepsilon_y^i, \end{aligned} \tag{4.15}$$

$$\begin{aligned} l_1\Delta\varepsilon_z^a + l_2\Delta\varepsilon_z^d + l_3\Delta\varepsilon_z^g &= l_1\Delta\varepsilon_z^b + l_2\Delta\varepsilon_z^e + l_3\Delta\varepsilon_z^h \\ &= l_1\Delta\varepsilon_z^c + l_2\Delta\varepsilon_z^f + l_3\Delta\varepsilon_z^i, \end{aligned} \tag{4.16}$$

where

$$l_1 = \sqrt{v_\mathrm{f}}, \quad l_2 = \sqrt{l_1^2 + v_\mathrm{m}} - l_1, \quad l_3 = 1 - l_1 - l_2, \tag{4.17}$$

with v_f and v_m denoting the fiber and the matrix volume fractions. Here, the fiber/matrix interface layer is not included in the matrix volume fraction. The deformation compatibility in the fiber direction is expressed as

$$\Delta\varepsilon_x^a = \Delta\varepsilon_x^b, \quad \Delta\varepsilon_x^b = \Delta\varepsilon_x^c, \tag{4.18}$$

$$\Delta\varepsilon_x^b = \Delta\varepsilon_x^e, \quad \Delta\varepsilon_x^d = \Delta\varepsilon_x^e, \tag{4.19}$$

$$\Delta\varepsilon_x^c = \Delta\varepsilon_x^f, \quad \Delta\varepsilon_x^f = \Delta\varepsilon_x^i, \quad \Delta\varepsilon_x^g = \Delta\varepsilon_x^h, \quad \Delta\varepsilon_x^h = \Delta\varepsilon_x^i. \tag{4.20}$$

Each subcell satisfies its own constitutive equation depending on the material behavior, as given below

$$\Delta\sigma_{ij}^n = E_{ijkl}^n \left(\Delta\varepsilon_{kl}^n - \alpha_{kl}^n \Delta\theta \right), \tag{4.21}$$

where α_{kl}^n is the coefficient of thermal expansion tensor, and $\Delta\theta$ is the temperature change. Furthermore, for elastoplastic deformation, the material property tensor, E_{ijkl}^n may be expressed as

$$[E_\mathrm{ep}] = [E_\mathrm{e}] - \frac{[E_\mathrm{e}]\{q\}\{q\}^\mathrm{T}[E_\mathrm{e}]}{H' + \{q\}^\mathrm{T}[E_\mathrm{e}]\{q\}}, \tag{4.22}$$

in which $[E_\mathrm{ep}]$ and $[E_\mathrm{e}]$ are the elastoplastic and elastic material property matrices, respectively, $\{q\}$ is computed from

$$\{q\} = \frac{\partial F}{\partial \sigma_{ij}^n}, \tag{4.23}$$

where F is the yield function, and H' is the slope of the stress vs. plastic strain plot.

The unit cell stress and strain increments are the volume average of the subcell stress and strain increments as follows

$$\Delta\overline{\sigma}_{ij} = \sum V^k \Delta\sigma_{ij}^k \tag{4.24}$$

and

$$\Delta\overline{\varepsilon}_{ij} = \sum V^k \Delta\varepsilon_{ij}^k, \tag{4.25}$$

where V^k is the volume fraction of the kth subcell. The subcell stresses and strains are related by the effective constitutive equation as below:

$$\Delta\overline{\sigma}_{ij} = \overline{E}_{ijkl}(\Delta\overline{\varepsilon}_{kl} - \overline{\alpha}_{kl}\Delta\theta). \tag{4.26}$$

Putting together the above equations results in the following expressions

$$[T]\{\Delta\varepsilon\} = \{f\}, \tag{4.27}$$

in which $[T]$ is the matrix containing material and geometric properties, $\{\Delta\varepsilon\}$ is the vector containing strain increments of all subcells, and vector $\{f\}$ is expressed as

$$\{f\}^{\mathrm{T}} = \left\{\{0\}^{\mathrm{T}} \quad \{\Delta\overline{\varepsilon}\}^{\mathrm{T}}\right\}. \tag{4.28}$$

Solving for $\{\Delta\varepsilon\}$ yields

$$\{\Delta\varepsilon\} = [R]\{f\} = [R_2]\{\Delta\overline{\varepsilon}\}, \tag{4.29}$$

where matrix $[R]$ consists of two submatrices as shown below:

$$[R] = [T]^{-1} = \left[[R_1] \quad [R_2]\right]. \tag{4.30}$$

Eventually, substitution of (4.29) into (4.21), and the resulting expression into (4.24) yield

$$[\overline{E}] = [V][E][R_2], \tag{4.31}$$

$$\{\overline{\alpha}\} = -[\overline{E}]^{-1}[V]\frac{[E][R_1]\{\Delta\tau\} - \{\tau\}}{\Delta\theta}. \tag{4.32}$$

Equation (4.31) gives the effective stiffness of the unidirectional composite. Here $[V]$ and $[E]$ are the matrices constructed from the volume fractions and the material properties of subcells, respectively. On the other hand, (4.32) is used to compute the effective coefficients of thermal expansion. The details of the derivation and explanation are provided in [4]. Equations (4.31) and (4.32) are utilized for the Stiffness Loop while (4.32) is necessary for the Stress Loop

$$\{\sigma\} = [E]([R_1]\{\Delta\tau\} + [R_2]\{\alpha^{\text{unit}}\}\Delta\theta) - \{\tau\}. \tag{4.33}$$

The above equation computes the microlevel stresses at the constituent material level.

Once the effective material properties of each unidirectional layer are calculated as discussed previously, the lamination theories are used to determine the overall properties of the stacked layer. Either the classical lamination or higher-order lamination theory may be used. If the interlayer delamination is to be included in the model, each layer needs to be modeled individually; or a partial stack of layers may be modeled. The Lamination Module will vary on a case-by-case basis.

4.3.3 Examples of Fibrous Composites

In the example discussed below, the fiber was assumed to be elastic with an elastic modulus of 420 GPa and Poisson's ratio of 0.25. The matrix was considered to be elastoplastic with elastic modulus 70 GPa, Poisson's ratio 0.33, yield strength 500 MPa, and linear hardening modulus 1.2 GPa. The effective material properties of the composite were computed for the elastic and plastic ranges for different fiber volume fractions. The "Fibrous Module" described in Sect. 4.3.2 was used for the computation, and the finite element analysis of the microscale analysis was also conducted for comparison. The finite element model considered the fiber and matrix discretely in detail. Figure 4.10 shows the effective stress–strain curve along the fiber direction for various ratios of fiber volume fractions. Both finite element and analytical results compare very well as shown in the figure. In general, the stress–strain curve is bilinear because of linear hardening of the matrix material after yielding. When there is a low-volume fraction of fibers, the bilinear characteristics are more obvious than a higher fiber volume fraction because the matrix plays more roles for the former compared to the latter. In other words, the matrix plastic deformation is more noticeable as the strain increases for a lower fiber volume fraction. On the other hand, a higher volume fraction shows a very small effect of the matrix plastic deformation. For the latter case, the stress–strain curve is very close to linear.

Figure 4.11 shows the effective stiffness of the composite in the transverse direction. As expected, the matrix material's plastic deformation affects significantly the transverse effective stiffness for the plastic strain range. When the fiber volume fraction is not large, both analytical and finite element solutions are close to each other even for the plastic range. As the fiber volume fraction increases, there is discrepancy between the

two solutions for the plastic strain rage. Figure 4.12 plots the effective longitudinal Poisson's ratio as a function of the applied strain for various fiber volume fractions. The figure shows that Poisson's ratios jump to near 0.5 for the range of plastic deformation.

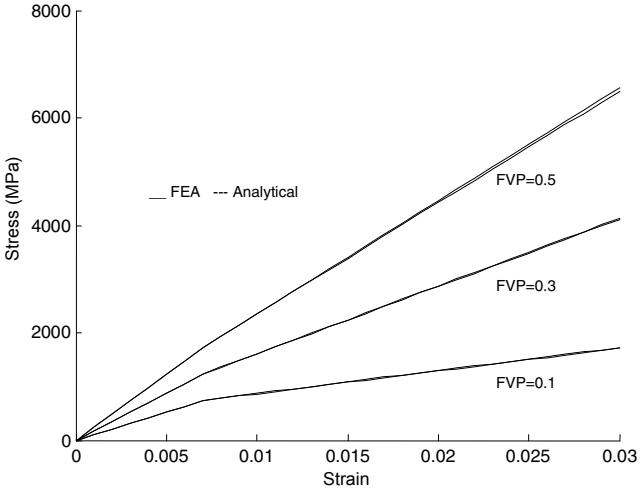

Fig. 4.10. Effective stress–strain plot in the longitudinal direction of a unidirectional fibrous composite for different fiber volume fractions

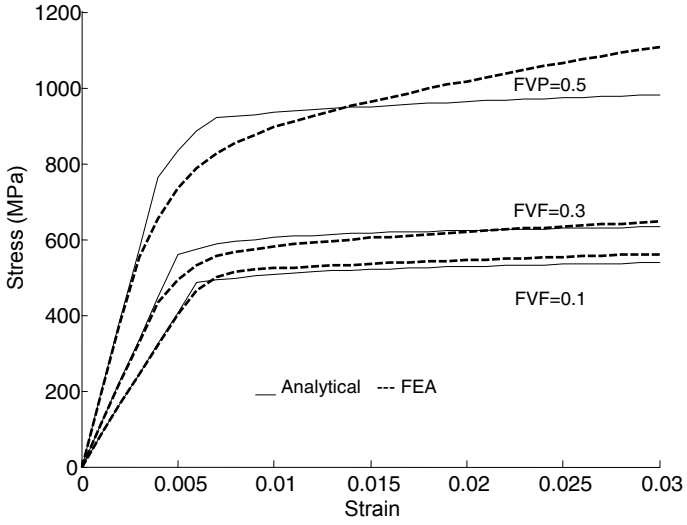

Fig. 4.11. Effective stress–strain plot in the transverse direction of a unidirectional fibrous composite for different fiber volume fractions

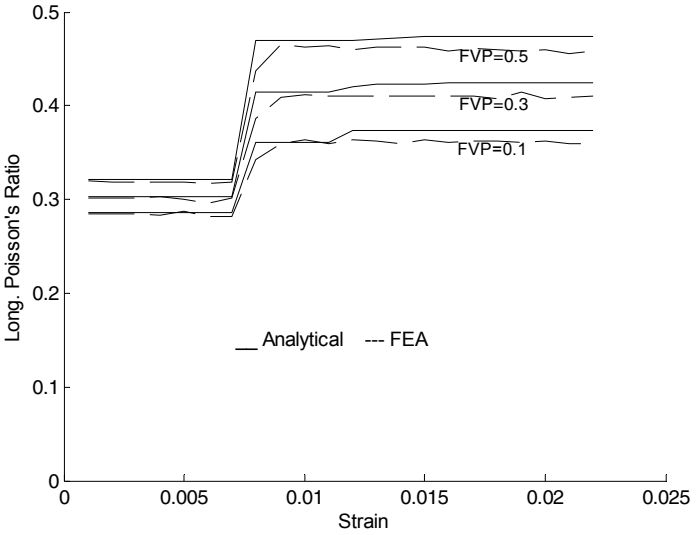

Fig. 4.12. Plot of strain vs. effective Poisson's ratio in the longitudinal direction of a unidirectional fibrous composite for different fiber volume fractions

4.4 Woven Fabric Composites

4.4.1 Multiscale Analysis for Woven Fabric Composites

Woven fabric composites have a more general analysis hierarchy than other kinds of composites. As a result, the analysis hierarchies for particulate and fibrous composites are special cases of those for woven fabric composites. Figure 4.13 illustrates the hierarchy for multiscale analysis of woven fabric composites. If the Fabric Module is omitted in Fig. 4.13, the procedure is the same as that for a fibrous composite. Because other modules were discussed previously, only the "Fabric Module" is presented here. The Fabric Module depends on the weaving pattern as sketched in Fig. 4.14. Because plain weave and twill weave are commonly used, Fabric Modules for those weave patterns are presented [8, 12, 18, 35].

4.4.2 Fabric Module for Plain Weave

The Fabric Module relates material properties of a unidirectional strand to the effective material properties of the woven fabric composite. Like the

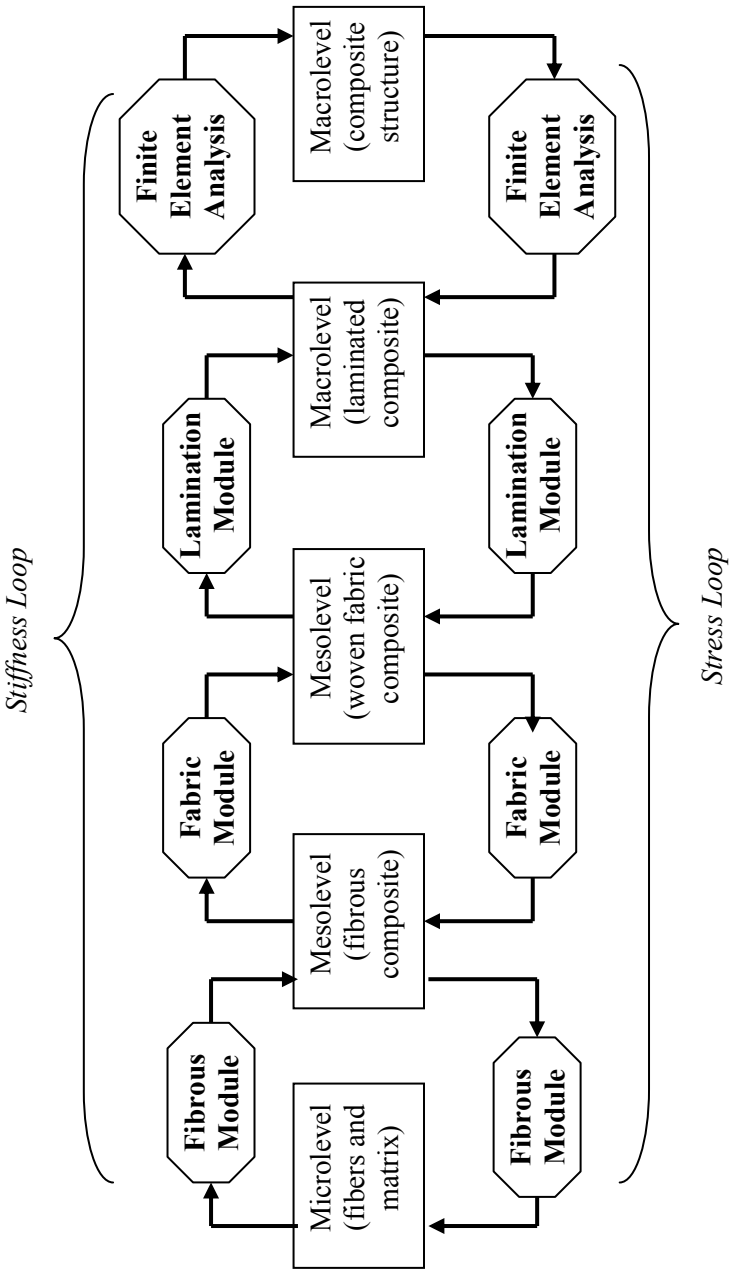

Fig. 4.13. Multiscale analysis hierarchy for a woven fabric composite

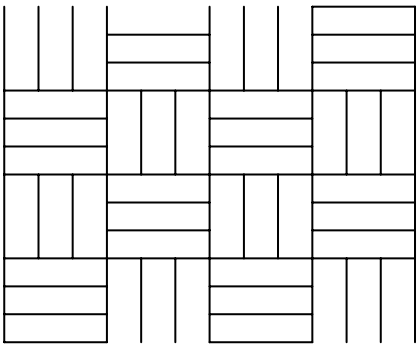

(**a**)

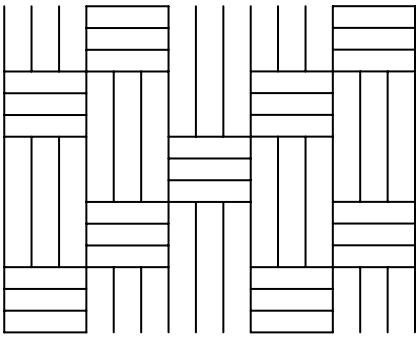

(**b**)

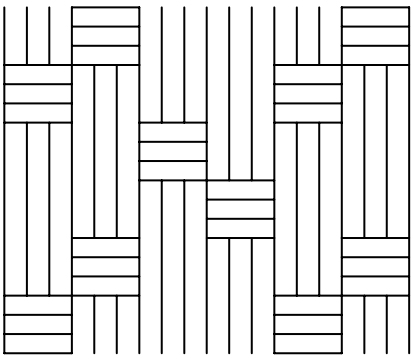

(**c**)

Fig. 4.14. Various weave patterns for woven fabric composites (**a**) Plain weave pattern (**b**) Twill weave pattern (**c**) Satin weave pattern

previous modules, this module has two functions: computation of the effective properties of the woven fabric using the strand materials and their weaving information, and decomposition of the woven strains and stresses into the strand strains and stresses. Plain weave is the simplest weave pattern of woven fabrics, as shown in Fig. 4.14. The representative unit cell for the plain weave is shown in Fig. 4.15.

The unit cell model for the plain weave has 13 subcells, and most of those subcells have fibers along the *x*- or *y*-axis. On the other hand, four subcells (*b*, *d*, *f*, and *h* in Fig. 4.15) have fibers in inclined orientations, and subcell *e* is filled with the matrix material.

First of all, the normal stress/strain components are discussed below. There are three normal strains for each subcell with the total of 39 strains ($(\varepsilon_{kl}^{\mathrm{str}})^n$, $n = a, b, \ldots, m$). There are three normal strains at the unit cell level ($\varepsilon_{kl}^{\mathrm{wf}}$). Those strains represent the average values of each subcell or the unit cell, respectively. To relate them, equilibrium and compatibility conditions are applied. At respective interfaces between any two neighboring subcells, the normal stresses on the interface plane should be in equilibrium.

$$(\sigma_x^{\mathrm{str}})^a = (\sigma_x^{\mathrm{str}})^b, \quad (\sigma_x^{\mathrm{str}})^b = (\sigma_x^{\mathrm{str}})^k, \tag{4.34}$$

$$(\sigma_x^{\mathrm{str}})^c = (\sigma_x^{\mathrm{str}})^j, \quad (\sigma_x^{\mathrm{str}})^d = (\sigma_x^{\mathrm{str}})^e, \tag{4.35}$$

$$(\sigma_x^{\mathrm{str}})^e = (\sigma_x^{\mathrm{str}})^f, \quad (\sigma_x^{\mathrm{str}})^g = (\sigma_x^{\mathrm{str}})^m, \tag{4.36}$$

$$(\sigma_x^{\mathrm{str}})^h = (\sigma_x^{\mathrm{str}})^i, \quad (\sigma_x^{\mathrm{str}})^i = (\sigma_x^{\mathrm{str}})^l, \tag{4.37}$$

$$(\sigma_y^{\mathrm{str}})^a = (\sigma_y^{\mathrm{str}})^l, \quad (\sigma_y^{\mathrm{str}})^d = (\sigma_y^{\mathrm{str}})^j, \tag{4.38}$$

$$(\sigma_y^{\mathrm{str}})^d = (\sigma_y^{\mathrm{str}})^g, \quad (\sigma_y^{\mathrm{str}})^b = (\sigma_y^{\mathrm{str}})^e, \tag{4.39}$$

$$(\sigma_y^{\mathrm{str}})^e = (\sigma_y^{\mathrm{str}})^h, \quad (\sigma_y^{\mathrm{str}})^c = (\sigma_y^{\mathrm{str}})^f, \tag{4.40}$$

$$(\sigma_y^{\mathrm{str}})^f = (\sigma_y^{\mathrm{str}})^m, \quad (\sigma_y^{\mathrm{str}})^i = (\sigma_y^{\mathrm{str}})^k, \tag{4.41}$$

$$(\sigma_z^{\mathrm{str}})^a = (\sigma_z^{\mathrm{str}})^j, \quad (\sigma_z^{\mathrm{str}})^c = (\sigma_z^{\mathrm{str}})^k, \tag{4.42}$$

$$(\sigma_z^{\mathrm{str}})^g = (\sigma_z^{\mathrm{str}})^l, \quad (\sigma_z^{\mathrm{str}})^i = (\sigma_z^{\mathrm{str}})^m, \tag{4.43}$$

where the superscript denotes the subcells in Fig. 4.15 and the subscript indicates the stress components. In addition, some strain compatibility conditions are assumed for a uniform deformation.

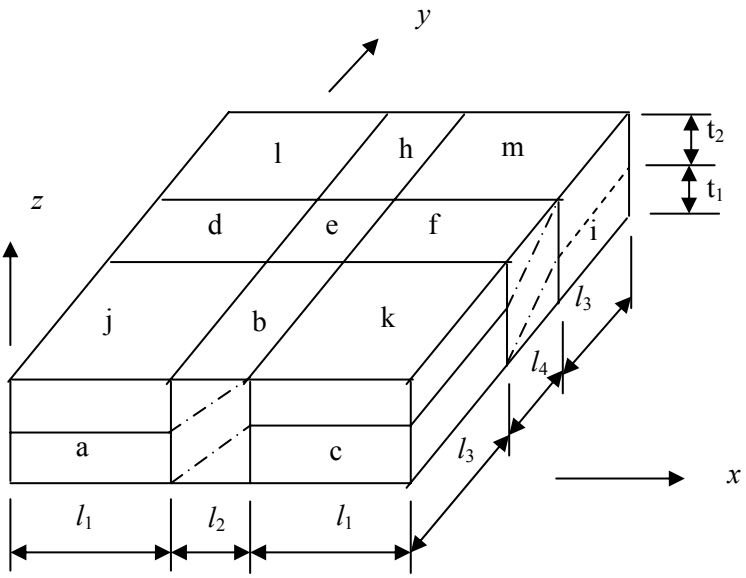

Fig. 4.15. Representative unit cell for the plain weave composite

$$(\varepsilon_x^{\mathrm{str}})^a + (\varepsilon_x^{\mathrm{str}})^k = (\varepsilon_x^{\mathrm{str}})^c + (\varepsilon_x^{\mathrm{str}})^j, \tag{4.44}$$

$$l_1(\varepsilon_x^{\mathrm{str}})^j + l_2(\varepsilon_x^{\mathrm{str}})^b + l_1(\varepsilon_x^{\mathrm{str}})^c = l_1(\varepsilon_x^{\mathrm{str}})^d + l_2(\varepsilon_x^{\mathrm{str}})^e + l_1(\varepsilon_x^{\mathrm{str}})^f, \tag{4.45}$$

$$l_1(\varepsilon_x^{\mathrm{str}})^d + l_2(\varepsilon_x^{\mathrm{str}})^e + l_1(\varepsilon_x^{\mathrm{str}})^f = l_1(\varepsilon_x^{\mathrm{str}})^g + l_2(\varepsilon_x^{\mathrm{str}})^h + l_1(\varepsilon_x^{\mathrm{str}})^m, \tag{4.46}$$

$$(\varepsilon_x^{\mathrm{str}})^g + (\varepsilon_x^{\mathrm{str}})^m = (\varepsilon_x^{\mathrm{str}})^i + (\varepsilon_x^{\mathrm{str}})^l, \tag{4.47}$$

$$(\varepsilon_y^{\mathrm{str}})^a + (\varepsilon_y^{\mathrm{str}})^l = (\varepsilon_y^{\mathrm{str}})^g + (\varepsilon_y^{\mathrm{str}})^j, \tag{4.48}$$

$$l_3(\varepsilon_y^{\mathrm{str}})^j + l_4(\varepsilon_y^{\mathrm{str}})^d + l_3(\varepsilon_y^{\mathrm{str}})^g = l_3(\varepsilon_y^{\mathrm{str}})^b + l_4(\varepsilon_y^{\mathrm{str}})^e + l_3(\varepsilon_y^{\mathrm{str}})^h, \tag{4.49}$$

$$l_3(\varepsilon_y^{\mathrm{str}})^b + l_4(\varepsilon_y^{\mathrm{str}})^e + l_3(\varepsilon_y^{\mathrm{str}})^h = l_3(\varepsilon_y^{\mathrm{str}})^c + l_4(\varepsilon_y^{\mathrm{str}})^f + l_3(\varepsilon_y^{\mathrm{str}})^m, \tag{4.50}$$

$$(\varepsilon_y^{\mathrm{str}})^c + (\varepsilon_y^{\mathrm{str}})^m = (\varepsilon_y^{\mathrm{str}})^i + (\varepsilon_y^{\mathrm{str}})^k, \tag{4.51}$$

$$t_1(\varepsilon_z^{\mathrm{str}})^a + t_2(\varepsilon_z^{\mathrm{str}})^j = (t_1 + t_2)(\varepsilon_z^{\mathrm{str}})^b, \tag{4.52}$$

$$t_1(\varepsilon_z^{\mathrm{str}})^c + t_2(\varepsilon_z^{\mathrm{str}})^k = (t_1 + t_2)(\varepsilon_z^{\mathrm{str}})^b, \tag{4.53}$$

$$t_1(\varepsilon_z^{\mathrm{str}})^c + t_2(\varepsilon_z^{\mathrm{str}})^k = (t_1 + t_2)(\varepsilon_z^{\mathrm{str}})^d, \tag{4.54}$$

$$(\varepsilon_z^{\mathrm{str}})^d = (\varepsilon_z^{\mathrm{str}})^e, \tag{4.55}$$

$$(\varepsilon_z^{\mathrm{str}})^e = (\varepsilon_z^{\mathrm{str}})^f, \tag{4.56}$$

$$t_1(\varepsilon_z^{\mathrm{str}})^g + t_2(\varepsilon_z^{\mathrm{str}})^l = (t_1 + t_2)(\varepsilon_z^{\mathrm{str}})^f, \tag{4.57}$$

$$t_1(\varepsilon_z^{\text{str}})^g + t_2(\varepsilon_z^{\text{str}})^l = (t_1 + t_2)(\varepsilon_z^{\text{str}})^h, \tag{4.58}$$

$$t_1(\varepsilon_z^{\text{str}})^i + t_2(\varepsilon_z^{\text{str}})^m = (t_1 + t_2)(\varepsilon_z^{\text{str}})^h. \tag{4.59}$$

Here, l_i and t_i are the dimensions of the plain weave construction as shown in Fig. 4.15. Finally, the unit cell strain and stress are assumed to be the volume average of the subcell strains and stresses, respectively. That is,

$$\varepsilon_{ij}^{\text{wf}} = \sum_{n=a,\ldots} V^n(\varepsilon_{ij}^{\text{str}})^n, \tag{4.60}$$

$$\sigma_{ij}^{\text{wf}} = \sum_{n=a\ldots} V^n(\sigma_{ij}^{\text{str}})^n. \tag{4.61}$$

Here, V^n is the volume fraction of the nth subcell. The constitutive equation for each subcell is expressed as

$$(\sigma_{ij}^{\text{str}})^n = (E_{ijkl}^{\text{str}})^n(\varepsilon_{kl}^{\text{str}})^n \quad (i,j,k,l = 1,2,3), \tag{4.62}$$

where the summation sign convention is applied only to the subscripts, k and l. For each subcell, $(E_{ijkl}^{\text{str}})^n$ should be determined based on the orientation of the strand inside the subcell. Algebraic manipulation of the previous equations, i.e., (4.34)–(4.62), yields the following relationship:

$$E_{ijkl}^{\text{wf}} = f\left((E_{ijkl}^{\text{str}})^n, l_i, t_i\right), \tag{4.63}$$

$$(\varepsilon_{ij}^{\text{str}})^n = g\left(\varepsilon_{ij}^{\text{wf}}, l_i, t_i\right). \tag{4.64}$$

Equations (4.63) and (4.64) are equivalent to (4.52) and (4.50) for the fiber-strand module, respectively. Equation (4.63) computes the effective material properties of the woven fabric composite based on the material and geometric properties of the strands while (4.64) calculates the strains at the strand level from the woven fabric strains. Once the strand strains are computed, strand stresses can be computed from the constituent equations.

A similar derivation can be made for shear components. For example, the shear component parallel to x–y plane can be derived as shown below. The shear stress equilibrium at the subcell interfaces is written as

$$t_1(\sigma_{xy}^{\text{str}})^a + t_2(\sigma_{xy}^{\text{str}})^j = (t_1 + t_2)(\sigma_{xy}^{\text{str}})^b, \tag{4.65}$$

$$t_1(\sigma_{xy}^{\text{str}})^c + t_2(\sigma_{xy}^{\text{str}})^k = (t_1 + t_2)(\sigma_{xy}^{\text{str}})^b, \tag{4.66}$$

$$t_1(\sigma_{xy}^{\text{str}})^a + t_2(\sigma_{xy}^{\text{str}})^j = (t_1 + t_2)(\sigma_{xy}^{\text{str}})^d, \tag{4.67}$$

$$t_1(\sigma_{xy}^{\text{str}})^g + t_2(\sigma_{xy}^{\text{str}})^l = (t_1 + t_2)(\sigma_{xy}^{\text{str}})^d, \tag{4.68}$$

$$t_1(\sigma_{xy}^{\text{str}})^g + t_2(\sigma_{xy}^{\text{str}})^l = (t_1 + t_2)(\sigma_{xy}^{\text{str}})^h, \tag{4.69}$$

$$t_1(\sigma_{xy}^{\text{str}})^i + t_2(\sigma_{xy}^{\text{str}})^m = (t_1 + t_2)(\sigma_{xy}^{\text{str}})^h, \tag{4.70}$$

$$t_1(\sigma_{xy}^{\text{str}})^i + t_2(\sigma_{xy}^{\text{str}})^m = (t_1 + t_2)(\sigma_{xy}^{\text{str}})^f, \tag{4.71}$$

$$(\sigma_{xy}^{\text{str}})^b = (\sigma_{xy}^{\text{str}})^e. \tag{4.72}$$

Assumed strain compatibility expressions are:

$$(\varepsilon_{xy}^{\text{str}})^a = (\varepsilon_{xy}^{\text{str}})^j, \tag{4.73}$$

$$(\varepsilon_{xy}^{\text{str}})^c = (\varepsilon_{xy}^{\text{str}})^k, \tag{4.74}$$

$$(\varepsilon_{xy}^{\text{str}})^g = (\varepsilon_{xy}^{\text{str}})^l, \tag{4.75}$$

$$(\varepsilon_{xy}^{\text{str}})^c = (\varepsilon_{xy}^{\text{str}})^i. \tag{4.76}$$

Use of (4.65)–(4.76) along with (4.60)–(4.62) for the shear component yields the shear component part of (4.63) and (4.64).

4.4.3 Fabric Module for 2/2-Twill Weave

The representative unit cell model for the 2/2-twill weave is sketched in Fig. 4.16. The unit cell was divided into 77 subcells. Of the 77 subcells, some were considered to have the same average stress states. The finite element model was run on several materials under a uniformed displacement to validate this assumption. Figure 4.17 is a schematic depiction of the subcells. Those having the same number designation are assumed to have the same average stress state. As a result, 17 independent subcells are used in the unit cell model. Forty-eight linearly independent equations were developed which relate the normal stresses and normal strains of the 17 uniquely stressed subcells. These 48 equations are the basis for the unit cell model. The average stress and strain of each subcell are used in all subsequent equations. The first set of equations represents the stress equilibrium at the subcell interfaces. Applying equilibrium to any two neighboring subcells results in the following normal stress equations, where the subscripts indicate stress components and the superscripts designate the subcell numbers.

The subsequent equations are a set of normal stress equilibriums in the 1-, 2-, and 3-directions, respectively

$$\begin{aligned}
&\sigma_{11}^{2}=\sigma_{11}^{8},\quad \sigma_{11}^{2}=\sigma_{11}^{15},\quad \sigma_{11}^{2}=\sigma_{11}^{14},\quad \sigma_{11}^{3}=\sigma_{11}^{7},\quad \sigma_{11}^{3}=\sigma_{11}^{15},\\
&\sigma_{11}^{3}=\sigma_{11}^{14},\quad \sigma_{11}^{5}=\sigma_{11}^{9},\quad \sigma_{11}^{4}=\sigma_{11}^{6},\quad \sigma_{11}^{1}=\sigma_{11}^{16},\quad \sigma_{11}^{1}=\sigma_{11}^{17},\\
&\sigma_{11}^{1}=\sigma_{11}^{10}+\sigma_{11}^{11},\quad \sigma_{11}^{1}=\sigma_{11}^{12}+\sigma_{11}^{13},
\end{aligned} \tag{4.77}$$

$$\begin{aligned}
&\sigma_{22}^{4}=\sigma_{22}^{16},\quad \sigma_{22}^{4}=\sigma_{22}^{17},\quad \sigma_{22}^{4}=\sigma_{22}^{12},\quad \sigma_{22}^{5}=\sigma_{22}^{17},\quad \sigma_{22}^{5}=\sigma_{22}^{17},\\
&\sigma_{22}^{5}=\sigma_{22}^{11},\quad \sigma_{22}^{3}=\sigma_{22}^{13},\quad \sigma_{22}^{2}=\sigma_{22}^{10},\quad \sigma_{22}^{1}=\sigma_{22}^{14},\quad \sigma_{22}^{1}=\sigma_{22}^{15},\\
&\sigma_{22}^{1}=\sigma_{22}^{6}+\sigma_{22}^{7},\quad \sigma_{22}^{1}=\sigma_{22}^{8}+\sigma_{22}^{9},
\end{aligned} \tag{4.78}$$

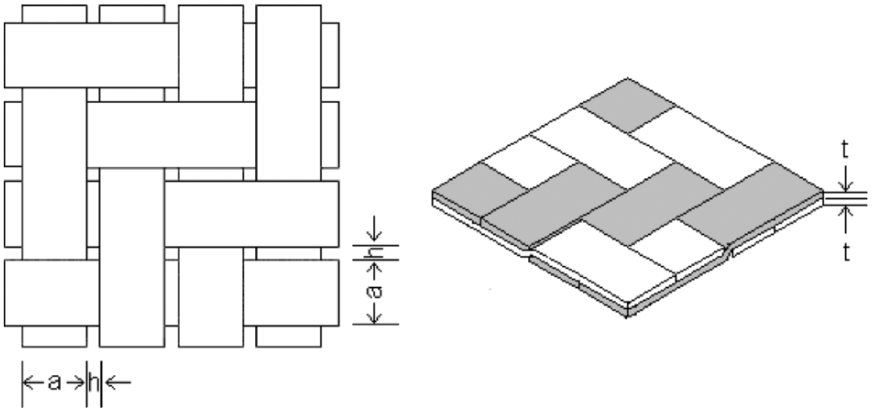

Fig. 4.16. Representative unit cell for 2/2-twill weave

2	8	2	15	3	7	3
	1		1		1	
3	14	2	8	2	15	3
13	1		1	10	1	
3	7	3	14	2	8	2
	1	13	1		1	10
2	15	3		3	14	2

Horizontal strand direction

5	9	5		4	6	4
16	1	11	1	17	1	12
4		5	9	5		4
12	1	16	1	11	1	17
4	6	4		5	9	5
17	1	12	1	16	1	11
5		4	6	4		5

Vertical strand direction

Fig. 4.17. Subcell numbering for the 2/2-twill unit cell

$$\begin{aligned} &\sigma_{33}^{2} = \sigma_{33}^{5}, \quad \sigma_{33}^{3} = \sigma_{33}^{4}, \quad \sigma_{33}^{6} = \sigma_{33}^{7}, \\ &\sigma_{33}^{8} = \sigma_{33}^{9}, \quad \sigma_{33}^{10} = \sigma_{33}^{11}, \quad \sigma_{33}^{12} = \sigma_{33}^{13}. \end{aligned} \tag{4.79}$$

The following equations represent the directional strain compatibility assuming a uniform deformation of the unit cell, where *a* and *h* are the dimensions of the fill and warp strands of the composite material, as shown in Fig. 4.17

$$\begin{aligned} &2a(\varepsilon_{11}^{2} + \varepsilon_{11}^{3}) + h(\varepsilon_{11}^{7} + \varepsilon_{11}^{8}) = 2a(\varepsilon_{11}^{4} + \varepsilon_{11}^{5}) + h(\varepsilon_{11}^{6} + \varepsilon_{11}^{9}), \\ &2a(\varepsilon_{11}^{2} + \varepsilon_{11}^{3}) + h(\varepsilon_{11}^{8}) = 2a(\varepsilon_{11}^{4} + \varepsilon_{11}^{5}) + h(\varepsilon_{11}^{9}), \\ &2a(\varepsilon_{11}^{2} + \varepsilon_{11}^{3}) + h(\varepsilon_{11}^{8} + \varepsilon_{11}^{14} + \varepsilon_{11}^{15}) = a(\varepsilon_{11}^{10} + \varepsilon_{11}^{13} + \varepsilon_{11}^{16} + \varepsilon_{11}^{17}) + 3h(\varepsilon_{11}^{1}), \\ &\varepsilon_{11}^{10} + \varepsilon_{11}^{12} = \varepsilon_{11}^{11} + \varepsilon_{11}^{13}, \end{aligned} \tag{4.80}$$

$$\begin{aligned} &2a(\varepsilon_{22}^{2} + \varepsilon_{22}^{3}) + h(\varepsilon_{22}^{11} + \varepsilon_{22}^{12}) = 2a(\varepsilon_{22}^{4} + \varepsilon_{22}^{5}) + h(\varepsilon_{22}^{10} + \varepsilon_{22}^{13}), \\ &2a(\varepsilon_{22}^{2} + \varepsilon_{22}^{3}) + h(\varepsilon_{22}^{13}) = 2a(\varepsilon_{22}^{4} + \varepsilon_{22}^{5}) + h(\varepsilon_{22}^{12}), \\ &2a(\varepsilon_{22}^{4} + \varepsilon_{22}^{5}) + h(\varepsilon_{22}^{12} + \varepsilon_{22}^{16} + \varepsilon_{22}^{17}) = a(\varepsilon_{22}^{6} + \varepsilon_{22}^{9} + \varepsilon_{22}^{14} + \varepsilon_{22}^{15}) + 3h(\varepsilon_{22}^{1}), \\ &\varepsilon_{22}^{6} + \varepsilon_{22}^{8} = \varepsilon_{22}^{7} + \varepsilon_{22}^{9}, \end{aligned} \tag{4.81}$$

$$\begin{aligned} &\varepsilon_{33}^{2} + \varepsilon_{33}^{5} = \varepsilon_{33}^{16}, \quad \varepsilon_{33}^{2} + \varepsilon_{33}^{5} = \varepsilon_{33}^{15}, \quad \varepsilon_{33}^{2} + \varepsilon_{33}^{5} = \varepsilon_{33}^{17}, \quad \varepsilon_{33}^{2} + \varepsilon_{33}^{5} = \varepsilon_{33}^{14}, \\ &\varepsilon_{33}^{2} + \varepsilon_{33}^{5} = \varepsilon_{33}^{1}, \quad \varepsilon_{33}^{2} + \varepsilon_{33}^{5} = \varepsilon_{33}^{6} + \varepsilon_{33}^{7}, \quad \varepsilon_{33}^{2} + \varepsilon_{33}^{5} = \varepsilon_{33}^{12} + \varepsilon_{33}^{13}, \\ &\varepsilon_{33}^{2} + \varepsilon_{33}^{5} = \varepsilon_{33}^{6} + \varepsilon_{33}^{8}, \quad \varepsilon_{33}^{2} + \varepsilon_{33}^{5} = \varepsilon_{33}^{10} + \varepsilon_{33}^{11}, \quad \varepsilon_{33}^{2} + \varepsilon_{33}^{5} = \varepsilon_{33}^{3} + \varepsilon_{33}^{4}. \end{aligned} \tag{4.82}$$

The constitutive equation for each subcell is given below in (4.83), where $(\sigma_{ij}^{\mathrm{str}})^{n}$ and $(\varepsilon_{kl}^{\mathrm{str}})^{n}$ are the *n*th subcell stresses and strains, and $(E_{ijkl}^{\mathrm{str}})^{n}$ is the subcell material property matrix in terms of the unit cell axes

$$(\sigma_{ij}^{\mathrm{str}})^{n} = (E_{ijkl}^{\mathrm{str}})^{n}(\varepsilon_{kl}^{\mathrm{str}})^{n}. \tag{4.83}$$

The stiffness matrix $(E_{ijkl}^{\mathrm{str}})^{n}$ is determined from stress and strain equations in conjunction with the proper transformation matrices.

A result of weaving is that fibers must be undulated. The undulation angle is measured from the plane in which the majority of the fibers lay straight. The undulated portions of the strand must have their material

properties adjusted to that of the global coordinate system. A brief explanation of stiffness transformation follows.

Let coordinate system x, y, and z be the global coordinate system, and x_1, y_1, and z_1 be the local coordinate system where the fiber in the strand of interest is aligned with the local axis. The stress and strain transformation from the local coordinates to global coordinates will be:

$$\begin{aligned} \{\sigma\}^{x_1y_1z_1} &= [T_\sigma]\{\sigma\}^{xyz}, \\ \{\varepsilon\}^{x_1y_1z_1} &= [T_\varepsilon]\{\varepsilon\}^{xyz}. \end{aligned} \tag{4.84}$$

The constitutive equations are:

$$\begin{aligned} \{\sigma\}^{xyz} &= [C]^{xyz}\{\varepsilon\}^{xyz}, \\ \{\sigma\}^{x_1y_1z_1} &= [C]^{x_1y_1z_1}\{\varepsilon\}^{x_1y_1z_1}. \end{aligned} \tag{4.85}$$

Mathematical manipulation of the above equations results in the following stiffness transformation equations

$$\begin{aligned} \{\sigma\}^{x_1y_1z_1} &= [C]^{x_1y_1z_1}[T_\varepsilon]\{\varepsilon\}^{xyz}, \\ [T_\sigma]\{\sigma\}_{kl}^{xyz} &= [C]^{x_1y_1z_1}[T_\varepsilon]\{\varepsilon\}^{xyz}, \\ \{\sigma\}^{xyz} &= [T_\sigma]^{-1}[C]^{x_1y_1z_1}[T_\varepsilon]\{\varepsilon\}^{xyz}, \\ \{\sigma\}^{xyz} &= [C]^{xyz}\{\varepsilon\}^{xyz}, \end{aligned} \tag{4.86}$$

where

$$[C]^{xyz} = [T_\sigma]^{-1}[C]^{x_1y_1z_1}[T_\varepsilon]. \tag{4.87}$$

Finally, the transformation matrices are as follows

$$[E_{ijkl}^{\text{str}}] = [T_\sigma]^{-1}[\overline{E}^{\text{str}}][T_\varepsilon], \tag{4.88}$$

where

$$[T_\varepsilon]^{-1} = \begin{bmatrix} m^2 & n^2 & 0 & 0 & 0 & mn \\ n^2 & m^2 & 0 & 0 & 0 & -mn \\ 0 & 0 & 1 & 0 & 0 & 0 \\ 0 & 0 & 0 & m & -n & 0 \\ 0 & 0 & 0 & n & m & 0 \\ -2mn & 2mn & 0 & 0 & 0 & m^2-n^2 \end{bmatrix}, \tag{4.89}$$

$$[T_\sigma]^{-1} = \begin{bmatrix} m^2 & n^2 & 0 & 0 & 0 & 2mn \\ n^2 & m^2 & 0 & 0 & 0 & -2mn \\ 0 & 0 & 1 & 0 & 0 & 0 \\ 0 & 0 & 0 & m & -n & 0 \\ 0 & 0 & 0 & n & m & 0 \\ -mn & mn & 0 & 0 & 0 & m^2 - n^2 \end{bmatrix}. \tag{4.90}$$

The matrices $[T_\sigma]$ and $[T_\varepsilon]$ are the stress and strain transformation matrices. Transformation matrices account for a reduction or increase in the composite's material properties when the composite is rotated with respect to the coordinate axes from which the property was measured.

The final equations describe the relationship between the woven fabric unit cell stresses (or strains) and the strand subcell stresses (or strains). The woven fabric unit cell stresses and strains are computed as volumetric average of subcell stresses and strains

$$\sigma_{ij}^{\text{wf}} = \sum_{n=1}^{17} V^n (\sigma_{ij}^{\text{str}})^n, \tag{4.91}$$

$$\varepsilon_{ij}^{\text{wf}} = \sum_{n=1}^{17} V^n (\varepsilon_{ij}^{\text{str}})^n, \tag{4.92}$$

where V^n is the volume fraction of the *n*th subcell. After manipulating all the equations, the following relationships result:

$$E_{ijkl}^{\text{wf}} = f\left((E_{ijkl}^{\text{str}})^n, a, h, t\right), \tag{4.93}$$

$$(\varepsilon_{ij}^{\text{str}})^n = g(\varepsilon_{ij}^{\text{wf}}, a, h, t). \tag{4.94}$$

These two equations provide the bidirectional passage of the strand-fabric module. Equation (4.93) is used to compute the effective woven fabric stiffness E_{ijkl}^{wf} of a 2/2-twill composite from the stiffness $(E_{ijkl}^{\text{str}})^n$ of unidirectional strand and the weave geometric dimensions *a*, *h*, and *t*. Additionally, (4.94) decomposes the 2/2-twill composite strains into the subcell strains. The subcell stresses can then be calculated using (4.83).

4.4.4 Examples of Woven Fabric Composites

First of all, the Fibrous Module and Fabric Module were tested independently. The Fibrous Module was validated extensively in previous works [7, 15, 23], and it was tested again for a carbon/epoxy strand. The fiber and matrix materials are shown in Table 4.1. The effective stiffness and strength properties of the strand made of the fiber and matrix materials in Table 4.1 and a fiber volume fraction of 0.7 are compared with the results in [2] and in Table 4.2.

Plain weave composites were studied using the strand-fabric module. (Material properties of the strands of the woven-fabric composites are tabulated in Table 4.3.) The calculated effective material properties are compared to other results in Tables 4.4 and 4.5 for the carbon/epoxy and e-glass/vinylester woven composites, respectively. The present results compared well to other experimental data or analytical results.

Another plain weave composite made of the strand in Table 4.2 was also studied for its tensile strength. The predicted strength using the fiber-strand and strand-fabric modules is compared to the test result in [2]. As shown in Table 4.6, the predicted strength agrees well with the test result.

Table 4.1. Properties of fiber and matrix materials

	E_1 (GPa)	E_2 (GPa)	G_{12} (GPa)	G_{23} (GPa)	γ_{12}	γ_{23}	Tensile strength (MPa)	Shear strength (MPa)
Fiber	221	3.8	13.8	5.5	0.20	0.25	3,585	
Matrix	4.4	4.4	1.6	1.6	0.34	0.34	159	100

Table 4.2. Properties of strand material

	E_1 (GPa)	E_2 (GPa)	γ_{12}	γ_{23}	Long. strength (MPa)	Trans. strength (MPa)
[28]	151.0	10.1	0.24	0.50	2,550	152
Present	156.0	10.2	0.24	0.54	2,543	148

Table 4.3. Material properties of strands and resin

	E_1 (GPa)	E_2 (GPa)	G_{12} (GPa)	G_{23} (GPa)	γ_{12}	γ_{23}
E-glass/ vinylester	57.5	18.8	7.44	7.26	0.25	0.29
Carbon/epoxy	134	10.2	5.52	3.43	0.30	0.49
Epoxy	3.45	3.45	1.28	1.28	0.35	0.35

Table 4.4. Comparison of plain weave composite made of carbon/epoxy

	E_1 (GPa)	E_2 (GPa)	G_{12} (GPa)	G_{23} (GPa)	γ_{12}	γ_{23}
Exp. [28]	55.5	–	4.93	–	0.06	–
Result [29]	56.1	10.4	5.08	3.71	0.03	0.59
Present result	54.9	10.2	4.28	3.47	0.02	0.47

Table 4.5. Comparison of plain weave composite made of e-glass/vinylester

	E_1 (GPa)	E_2 (GPa)	G_{12} (GPa)	G_{23} (GPa)	γ_{12}	γ_{23}
Exp. [30]	24.8	8.5	6.5	4.2	0.1	0.28
Result [30]	25.3	13.4	5.19	5.24	0.12	0.29
Present result	24.4	12.4	5.92	4.52	0.12	0.28

Table 4.6. Plain weave and woven fabric composite

	Tensile strength (MPa)
Present	753
[28]	750

The next study was a plain weave composite plate subjected to a bending load. A quarter of the plate was modeled with two symmetric planes. The fiber and matrix properties are listed in Table 4.1. The longitudinal fiber stresses were computed for a square simply supported plate with a uniform unit pressure loading because they are the ultimate load carrying elements. The magnitudes of fiber-carrying stresses and their contour plots are shown in Fig. 4.18.

Laminated composite plates made of a 2/2-twill composite with a center hole were analyzed next. The objective was to simulate failure initiation and progression of 2/2-twill woven fabric composite plates with drilled holes at the center. Plates with three different hole sizes were considered. The hole diameters were 3, 6, and 9 mm. Figure 4.19 shows quarter of each plate with finite element meshes.

A finite element model of the plates contained 143 nodes and 240 two-dimensional triangular elements. Because of symmetry, only a quarter of each plate was modeled. Symmetric boundary conditions were applied to the bottom and left boundaries; the inner radius was left free; and a uniform displacement was applied along the right boundary of the mesh.

The applied load was incrementally increased until the failure criterion was realized in the element of interest. In this case, the elements of interest

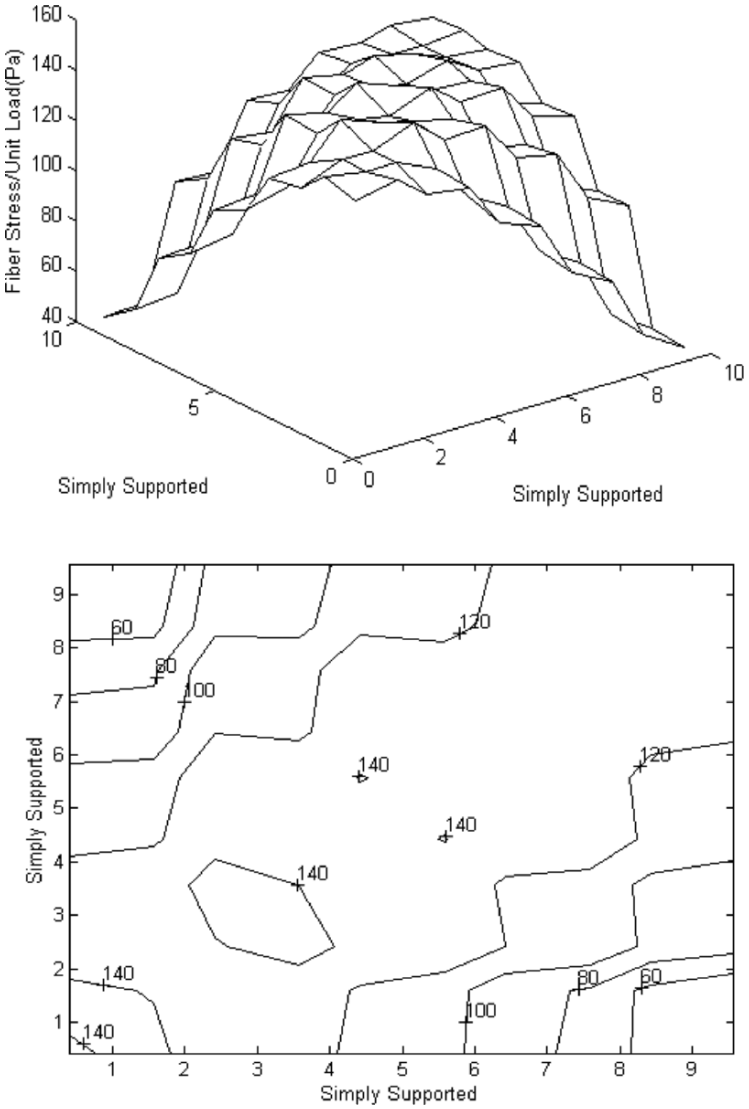

Fig. 4.18. Plot of fiber stresses for a square, simply supported plate made of a plain weave composite subjected to a uniform pressure loading

are those corresponding to the virtual strain gage in Fig. 4.19. Because of the high-volume fraction of the fibers, the ultimate strength of the fibers was set as the failure criterion for this analysis. With every incremental increase in applied strain, the multiscale model was used to determine the stresses in the fibers. Whenever a fiber reached its ultimate strength, the

material property at the point degraded in the finite element model. The results are tabulated in Table 4.7. The ultimate failure strengths of the three composite plates with circular holes were predicted using the present analysis model and compared to the experimental data [36]. The predicted strengths are close to both experimental and previously predicted results.

Since a gross assumption of the unit cell model is that the strains are constant in each subcell, it may be of interest to determine how the subcell strains compare to the average strains in the subcells of a detailed finite element model. The following strains were applied to the woven fabric for the sake of analysis

$$\varepsilon_{ii}^{\mathrm{wf}} = \left\{0.0160 \quad -0.0009 \quad 0\right\}^{\mathrm{T}}.$$

The finite element model was divided into volumes which corresponded to the subcells of the unit cell model. The finite element volume strains were determined in two ways. First, the average of the strains for all elements contained in the finite element volume was calculated. As a second check, an average nodal displacement on two opposing faces was calculated. The difference in the average nodal displacement for each face was divided by the original face length to determine an average strain in the volume. Only the strains in the direction of applied stress were compared, the *y*-direction for this case.

Three subcells were chosen for comparison with the finite element model. Those comparisons are tabulated in Table 4.8. The subcell numbers correspond to the number in Fig. 4.17. Both models agreed very well.

Table 4.7. Predicted and experimental strength of 2/2-twill composites with holes

Hole diameter (mm)	Experimental strength (MPa) [31]	Predicted strength (MPa)
3	435	494
6	395	438
9	333	354

Table 4.8. Comparison of subcell strains between the present unit cell and detailed finite element models

Subcell no.	Unit cell model	Finite element model
1	0.0221	0.0277
4	0.0165	0.0142
11	0.0164	0.0150

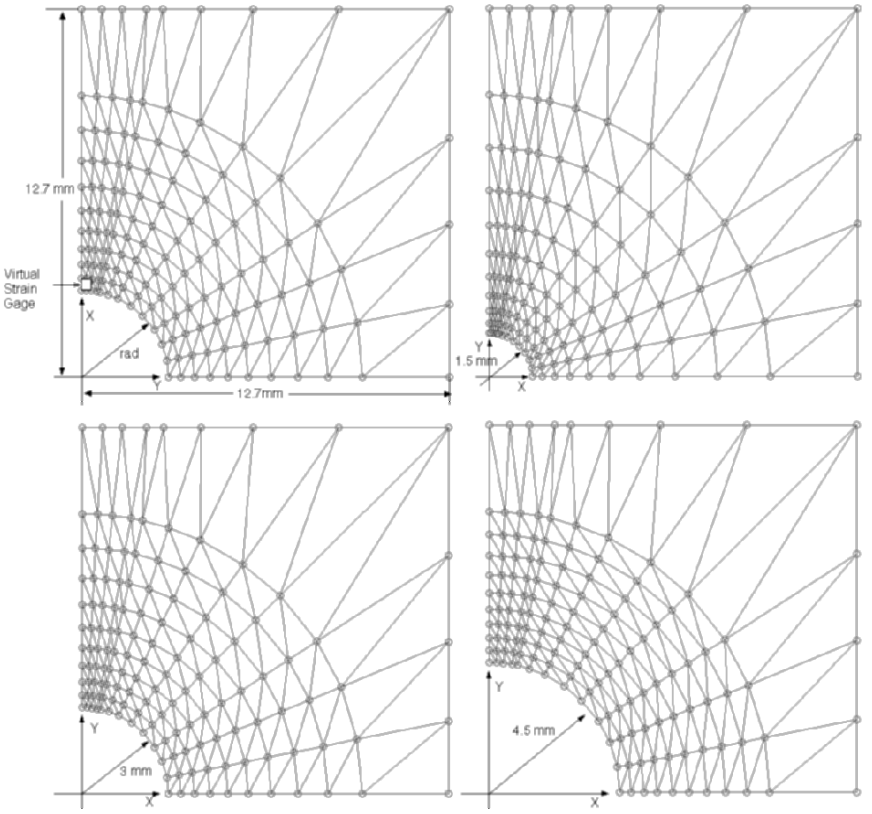

Fig. 4.19. Finite element mesh of quarters of plates with circular holes

4.5 Conclusions

Multiscale analysis techniques become increasingly important as we continuously strive to stretch composite material properties up to their ultimate limits. In that aspect, we may want to design and build composites starting from the atomic level [9, 11, 21, 22, 33, 34]. In this case, the multiscale techniques presented here should be extended to implement nanoscale characteristics. Otherwise, the present techniques are useful to design and analyze various composite structures from micro- to macroscale of engineering applications.

Acknowledgments

The author expresses his sincere gratitude to his graduate students and visiting scholars who have participated in the research projects presented in this manuscript.

References

1. Aitharaju VR, Averill RC (1999) Three-dimensional properties of woven-fabric composites. Composites Science and Technology 59: 1901–1911
2. Blackketter DM, Walrath DE, Hansen AC (1993) Modeling damage in a plain weave fabric-reinforced composite material. Journal of Composites Technology & Research 15: 136–142
3. Kwon YW (1991) Elasto-viscoplastic analysis of fiber-reinforced composites. Engineering Computations 8: 273–284
4. Kwon YW (1991) Material nonlinear analysis of composite plate bending using a new finite element formulation. Computers & Structures 41: 1111–1117
5. Kwon YW (1992) Finite element analysis of thermoelastoplastic stresses in composites. European Journal of Mechanical Engineering 37: 83–88
6. Kwon YW (1992) Thermo-elastoviscoplastic finite element plate bending analyses of composites. Engineering Computations 9: 595–607
7. Kwon YW (1993) Calculation of effective moduli of fibrous composites with micro-mechanical damages. Composite Structures 25: 187–192
8. Kwon YW (2001) Multi-level approach for failure in woven fabric composites. Advanced Engineering Materials 3: 713–717
9. Kwon YW (2003) Discrete atomic and smeared continuum modeling for static analysis. Engineering Computations 20: 964–978
10. Kwon YW (2005) Micromechanical, thermomechanical study of a refractory fiber/matrix/coating system. Journal of Thermal Stresses 28: 439–453
11. Kwon YW (2005) Multiscale modeling of mechanical behavior of polycrystalline materials. Journal of Computer-Aided Materials Design 11: 43–57
12. Kwon YW, Altekin A (2002) Multi-level, micro–macro approach for analysis of woven fabric composites. Journal of Composite Materials 36: 1005–1022
13. Kwon YW, Baron DT (1998) Numerical predictions of progressive damage evolution in particulate composites. Journal of Reinforced Plastics and Composites 17: 691–711

14. Kwon YW, Berner JM (1994) Analysis of matrix damage evolution in laminated composite plates. Engineering Fracture Mechanics 48: 811–817
15. Kwon YW, Berner JM (1995) Micromechanics model for damage and failure analyses of laminated fibrous composites. Engineering Fracture Mechanics 52: 231–242
16. Kwon YW, Berner JM (1997) Matrix damage analysis of fibrous composites: effects of thermal residual stresses and layer sequences. Computers & Structures 64: 375–382
17. Kwon YW, Byun KY (1990) Development of a new finite element formulation for the elasto-plastic analysis of fiber reinforced composites. Computers & Structures 35: 563–570
18. Kwon YW, Cho WM (2004) Multiscale thermal stress analysis of woven fabric composite. Journal of Thermal Stresses 27: 59–73
19. Kwon YW, Craugh LE (2001) Progressive failure modeling in notched cross-ply fibrous composites. Applied Composite Materials 8: 63–74
20. Kwon YW, Eren H (2000) Micromechanical study of interface stresses and failure in fibrous composites using boundary element method. Polymers & Polymer Composites 8: 369–386
21. Kwon YW, Harrell AF (2004) How many monomer repeat units are necessary for reliable molecular dynamics simulation. Polymers & Polymer Composites 12: 483–489
22. Kwon YW, Jung SH (2004) Atomic model and coupling with continuum model for static equilibrium problems. Computers & Structures 82: 1993–2000
23. Kwon YW, Kim C (1998) Micromechanical model for thermal analysis of particulate and fibrous composites. Journal of Thermal Stresses 21: 21–39
24. Kwon YW, Lee JH, Liu CT (1997) Modeling and simulation of crack initiation and growth in particulate composites. Transactions of the ASME: Journal of Pressure Vessel Technology 119: 319–324
25. Kwon YW, Lee JH, Liu CT (1998) Study of damage and crack in particulate composites. Composites Part B: Engineering 29: 443–450
26. Kwon YW, Liu CT (1997) Study of damage evolution in composites using damage mechanics and micromechanics. Composite Structures 38: 133–139
27. Kwon YW, Liu CT (1998) Damage growth in a particulate composite under a high strain rate loading. Mechanics Research Communications 25: 329–336
28. Kwon YW, Liu CT (1998) Effects of non-uniform particle distributions on damage evolution in pre-cracked, particulate composite specimens. Polymers & Polymer Composites 6: 387–397
29. Kwon YW, Liu CT (1999) Numerical study of damage growth in particulate composites. Transactions of the ASME: Journal of Engineering Materials and Technology 121: 476–482

30. Kwon YW, Liu CT (2000) Prediction of initial crack size in particulate composites with a circular hole. Mechanics Research Communications 27: 421–428
31. Kwon YW, Liu CT (2001) Effect of particle distribution on initial cracks forming from notch tips of composites with hard particles embedded in a soft matrix. Composites Part B: Engineering 32: 199–208
32. Kwon YW, Liu CT (2003) Microstructural effects on damage behavior in particle reinforced composites. Polymers & Polymer Composites 11: 1–8
33. Kwon YW, Manthena C (2006) Homogenization technique of discrete atoms into smeared continuum. Internal Journal of Mechanical Sciences 48: 1352–1359
34. Kwon YW, Manthena C, Oh JJ, Srivastava D (2005) Vibrational characteristics of carbon nanotubes as nanomechanical resonators. Journal of Nanoscience and Nanotechnology 5: 703–712
35. Kwon YW, Roach K (2004) Unit-cell model of 2/2-twill woven fabric composites for multiscale analysis. Computer Modeling in Engineering and Sciences 5: 63–72
36. Ng S, Tse P, Lau K (1998) Progressive failure analysis of 2/2-twill weave fabric composites with moulded-in circular hole. Composites Part B: Engineering 32: 139–152
37. Scida D, Aboura Z, Benzeggagh MM, Bocherens E (1999) A micromechanics model for 3d elasticity and failure of woven-fibre composite materials. Composites Science and Technology 59: 505–517